Fast microwave-induced thermoacoustic microscopic imaging based on one-dimensional galvanometer scanning*

NIE Yinqiang[1], CHI Zihui[2, 3, *], CHEN Lei[1], MENG Yang[1, 3], JIANG Huabei[4, *]

1. School of Electronic Science and Engineering, Chongqing University of Posts and Telecommunications, Chongqing 400065, China
2. School of Integrated Circuits, Chongqing University of Posts and Telecommunications, Chongqing 400065, China
3. Postdoctoral Research Center of Chongqing Key Laboratory of Photoelectronic Information Sensing and Transmitting Technology, Chongqing University of Posts and Telecommunications, Chongqing 400065, China
4. Department of Medical Engineering, University of South Florida, Tampa 33620, USA

Abstract

Microwave-induced thermoacoustic imaging, as an emerging biomedical imaging technique, combines the high contrast of microwave imaging with the high spatial resolution of ultrasound imaging. Microwave-induced thermoacoustic microscopy, as an important branch of this technology, retains these advantages while possessing the ability to visualize finer tissue characteristics. However, traditional raster scanning mechanisms introduce interference into microwave field distribution due to mechanical motion, thus necessitating multiple signal average to maintain signal-to-noise ratio. Additionally, the idle time during motor movement results in extended single-scan durations, limiting its practical applications. To address these limitations, this work proposes a rapid imaging system based on one-dimensional galvanometer scanning. The system employs a hybrid galvanometer-translation stage architecture and an optimized scanning strategy to minimize microwave field interference, reduce the number of signal averages and shortens the idle time, ultimately achieving more than a tenfold improvement in imaging speed. A specially designed timing control algorithm ensures the precise synchronization of microwave excitation, galvanometer motion, and ultrasound detection, while the reconstruction algorithm suitable for the optimizing scanning method effectively corrects

* The paper is an English translated version of the original Chinese paper published in Acta Physica Sinica. Please cite the paper as: NIE Yinqiang[1], CHI Zihui[2, 3, *], CHEN Lei[1], MENG Yang[1, 3], JIANG Huabei[4, *], **Fast microwave-induced thermoacoustic microscopic imaging based on one-dimensional galvanometer scanning**. *Acta Phys. Sin.*, 2026, 75(2):021001. doi: 10.7498/aps.75.20251014

distortions generated in the scanning process. The system performance is assessed through phantom and ex vivo tissue experiments. Resolution tests show hundred-micrometer resolution along all three axes (332 μm × 324 μm × 79 μm), while contrast and depth imaging experiments confirm its ability to clearly distinguish targets with different conductivities, achieving an effective detection depth of at least 10 mm in tissue. Early tumor mimicking experiments further demonstrate the ability of the system to identify lesion boundaries, preliminarily revealing its potential for rapid tumor margin assessment. This approach maintains the imaging quality of microwave-induced thermoacoustic microscopy while enhancing imaging efficiency and system stability, thereby laying a crucial foundation for advancing the technology from laboratory research to clinical applications.

Keywords: microwave-induced thermoacoustic imaging; microwave-induced thermoacoustic microscopy; galvanometer scanning; imaging speed
PACS: 07.05.Pj; 87.85.Pq; 87.57.-s; 87.57.C-

DOI: 10.7498/aps.75.20251014

cstr: 32037.14.aps.75.20251014

1 Introduction

Microwave-induced thermoacoustic imaging (MITAI) is an emerging biomedical imaging modality that integrates the high contrast of microwave imaging with the high resolution of ultrasound imaging. This technique detects thermoacoustic signals generated when biological tissues absorb microwave energy, thereby fusing functional information from microwave absorption with structural information from acoustic imaging. The origins of MITAI trace back to the late 19th century. In 1880, Bell[1] first discovered the photoacoustic effect. In 1983, Olsen and Lin[2] explored thermoacoustic imaging using pulsed microwave radiation. In 1999, Kruger et al.[3] achieved the first thermoacoustic breast imaging at 434 MHz. In 2000, Ku and Wang[4] made significant improvements to the MITAI system and systematically analyzed thermoacoustic signal characteristics, image resolution, and contrast. In recent years, extensive research by multiple groups has yielded a series of important advances in MITAI system design[5-10], imaging algorithms[11-17], and practical applications[18-26].

Microwave-induced thermoacoustic microscopy (MITAM), as a key branch of MITAI, further enhances the capability to observe fine tissue structures while inheriting the advantages of MITAI. However, MITAM remains in its early developmental stage. In

2012, Lou et al.[27] first employed nanosecond-pulse-width microwave pulses as the excitation source and successfully achieved high-resolution thermoacoustic imaging. Nevertheless, this approach relies on megawatt-level high-voltage pulsed microwave sources based on spark-gap switches, which are costly and suffer from timing jitter, limiting their widespread adoption in MITAI. In 2023, Fang et al.[28] developed a MITAM system by combining 70 ns short-pulse microwave excitation with a 25 MHz high-frequency focused ultrasound transducer, achieving a three-dimensional spatial resolution of 135 μm × 135 μm × 68 μm. They validated system performance using ex vivo imaging of scleroderma tissue. However, this system still faces challenges including slow imaging speed, low signal-to-noise ratio (SNR), and non-uniform field distribution. Specifically, the slow speed stems from interference caused by the conventional raster scanning mechanism with the microwave field. To maintain adequate SNR, extensive signal averaging (typically exceeding 500 averages) is required. Additionally, the settling time for motor stage movement (approximately 0.2 s per step) severely limits imaging efficiency. For example, with a pulse repetition frequency of 100 Hz, a step size of 0.14 mm × 0.2 mm, and a field of view of 5 mm × 5 mm, a single B-scan frame requires 187 s, and a full volumetric scan takes as long as 4680 s (approximately 1.3 h), significantly hindering practical utility.

To address this speed bottleneck, this study proposes a novel scanning strategy based on the conventional raster scanning architecture to enhance imaging speed and validate its feasibility. The system employs a hybrid scanning mechanism combining galvanometer mirrors and a translation stage. By optimizing the scanning protocol, the number of required transducer movements-traditionally performed by the translation stage-is reduced from 900 to 36 (for a step size of 0.14 mm × 0.2 mm and a 5 mm × 5 mm field of view). This reduction minimizes interference with the microwave field inherent in conventional raster scanning. The diminished interference reciprocally mitigates the adverse impact of microwave field instability on the system, thereby reducing the need for extensive signal averaging. Simultaneously, the high-speed capability of the galvanometer mirrors substantially shortens the dead time during scanning, collectively improving imaging efficiency. Compared with laser Doppler vibrometer-based galvanometers-which offer higher precision but are more susceptible to interference-this study adopts a laser marking galvanometer with positioning accuracy better than 0.01 mm, which fully satisfies the requirement of the 0.14 mm × 0.2 mm sampling step size. Moreover, its superior scanning speed provides headroom for future high-speed imaging implementations. In contrast to the MEMS (micro-electro-mechanical systems) galvanometers commonly used in photoacoustic microscopy[29,30], the laser marking galvanometer employed here[31] offers a larger imaging range and lower cost. Its mechanically isolated

structure-separating the motor from the mirror-facilitates effective electromagnetic shielding, thereby suppressing interference induced by high-frequency electromagnetic fields and preventing control signal inaccuracies. Furthermore, owing to its physically separable design, stronger drive signals, and inherent shielding from a metal housing, the laser marking galvanometer demonstrates superior adaptability in complex electromagnetic environments. Under this hybrid scanning architecture, the system-equipped with a self-developed control algorithm and a scanning distortion correction reconstruction method-exhibits excellent imaging performance in phantom and early tumor simulation experiments. The experimental results show strong agreement with theoretical analyses, physical photographs, or ultrasound images. Overall, this study achieves more than a tenfold increase in imaging speed while preserving image quality, with greater advantages becoming more pronounced as the field of view increases. This work preliminarily validates the potential of one-dimensional galvanometer scanning in MITAM and lays the groundwork for future development of even faster scanning approaches, such as two-dimensional galvanometer scanning and polygon mirror scanning.

2 Fundamental Theory

2.1 Generation Mechanism of Microwave-Induced Thermoacoustic Signals

When biological tissue is irradiated by a short microwave pulse, it absorbs microwave energy, leading to localized temperature rise. This thermal expansion subsequently generates thermoelastic stress, which radiates acoustic waves. In a medium with uniform acoustic and thermal properties, this acoustic wave generation process can be described by Equation (1)[32]:

$$\nabla^2 p(\boldsymbol{r},t) - \frac{1}{c^2}\frac{\partial^2 p(\boldsymbol{r},t)}{\partial t^2} = -\frac{\beta_e}{C_p}\frac{\partial H(\boldsymbol{r},t)}{\partial t}, \tag{1}$$

Here, $H(\boldsymbol{r},t)$ denotes the heating function at position **r** and time t, c represents the speed of sound, β_e is the thermal expansion coefficient of the material, C_p denotes the specific heat capacity at constant pressure, and $p(\boldsymbol{r},t)$ represents the acoustic pressure at position **r** and time t. This quantity also constitutes a solution to the wave equation and can be expressed by Equation (2)[33]:

$$\begin{aligned} p(\boldsymbol{r},t) &= \frac{\beta}{4\pi C_p}\iiint \frac{\partial H(\boldsymbol{r}',t')}{\partial t'}\frac{d^3\boldsymbol{r}}{|\boldsymbol{r}-\boldsymbol{r}'|}\Big|_{t'=t-|\boldsymbol{r}-\boldsymbol{r}'|/v} \\ &= \frac{\beta I_0 c^2 \tau}{4\pi C_p}\text{□}\int\int_{s|r-r'|=vt} A(\boldsymbol{r}')\frac{\mathrm{d}\boldsymbol{r}'}{t}, \end{aligned} \tag{2}$$

Here, τ denotes the microwave pulse duration, $A(r')$ represents the spatial microwave absorption coefficient, and I_0 is the incident pulse microwave energy density. Equation (2) indicates that the magnitude of the microwave-induced thermoacoustic signal received by the probe depends on the magnitude of the absorbed microwave energy density.

To characterize microwave absorption properties, the attenuation constant can be used as an approximate descriptor, as shown in Equation (3)[34]:

$$\partial = \omega \sqrt{\frac{\mu\omega}{2}[\sqrt{1+(\frac{\sigma}{\omega\varepsilon})^2}-1]}, \quad (3)$$

Here, ω denotes the microwave angular frequency, μ represents magnetic permeability, ε denotes permittivity, and σ represents electrical conductivity.

Theoretical analysis indicates that, under uniform excitation electric field conditions, differences in the dielectric properties-specifically, differences in equivalent electrical conductivity-within biological tissues constitute the endogenous contrast mechanism for microwave-induced thermoacoustic imaging. Consequently, functional imaging of biological tissues can be achieved through microwave-induced thermoacoustic imaging[35].

2.2 Factors Influencing the Resolution of Microwave Thermoacoustic Microscopy

The acoustic pressure of the thermoacoustic signal in Equation (1) can be expressed using the scalar potential of the velocity field, as shown in Equation (4):

$$p(\boldsymbol{r},t) = -\rho\frac{\partial}{\partial t}\phi(\boldsymbol{r},t). \quad (4)$$

When considering only the one-dimensional problem in the *z* direction, Equation (1) can be rewritten as Equation (5)[10]:

$$\frac{\partial^2}{\partial t^2}\phi(z,t) - c^2\Delta\phi(z,t) = (\frac{\beta \mathrm{v}^2}{\rho C})\mathrm{div}S, \quad (5)$$

Here, $\phi(z,t)$ denotes the scalar potential of the velocity field, *c* represents the speed of sound, and div$S$ indicates the divergence of the incident microwave Poynting vector. The one-dimensional Poynting vector can be expressed as $S = I_0 \mathrm{e}^{-\mu_a z} f(t) n_z$, where I_0 denotes the microwave excitation intensity, μ_a represents the absorption coefficient, z denotes depth, n_z is the unit vector in the *z*-axis direction, and $f(t)$

describes the temporal dependence of the microwave. Consequently, Equation (5) can be further expressed as Equation (6)[36]:

$$\frac{\partial^2\phi(z,t)}{\partial t^2} - c^2\frac{\partial^2\phi(z,t)}{\partial z^2} = -(\frac{\mu_a\beta v^2}{\rho C})I_0 e^{-\mu_a z} f(t). \quad (6)$$

Applying the Fourier transform to both sides of Equation (6) yields the thermoacoustic signal under Gaussian pulse excitation with a microwave pulse width of τ, as described by Equation (7)[27,37].

$$p(\tau,t) = -\frac{I_0\mu_a\beta c^2}{2C_p}\int_{-\infty}^{\infty} f(t)e^{-\mu_a c|\tau-t|}\mathrm{sgn}(\tau-t)\mathrm{d}t. \quad (7)$$

According to Equation (7), the temporal profile of the thermoacoustic pressure depends on the microwave pulse width: the narrower the microwave pulse width, the shorter the duration of the thermoacoustic signal and the higher the image resolution. Therefore, in microwave-induced thermoacoustic microscopy, the axial resolution along the *Z*-axis is primarily determined by the microwave pulse width and can be estimated using Equation (8)[27]:

$$d = \tau c. \quad (8)$$

In microwave-induced thermoacoustic microscopy, a point-focused transducer is employed for signal acquisition to achieve higher sensitivity. The diameter of its focal spot determines the diffraction-limited resolution in the *XY* plane, as described theoretically by Equation (9)[38,39]:

$$\mathrm{BD} = 1.02\frac{Fc}{fD}, \quad (9)$$

Here, BD denotes the beam spot diameter, F represents the transducer focal length, c denotes the speed of sound in the medium, f is the ultrasound frequency, and D represents the probe aperture. It should be specifically noted that, during actual imaging, the system's final lateral (i.e., *XY*-plane) resolution is jointly determined by the scanning step angle and the beam spot diameter.

2.3 Interference of Metals with the Microwave Field

The behavior of the probe under the influence of the microwave field can be described by the following electromagnetic frequency-domain governing equation:

$$\nabla\times\mu_r^{-1}(\nabla\times E(\boldsymbol{r})) - k_0^2(\varepsilon_r - \frac{j\sigma}{\omega\varepsilon_0})E(\boldsymbol{r}) = 0, \quad (10)$$

Here, μ_r denotes the relative permeability, $E(\boldsymbol{r})$ represents the electric field intensity vector, k_0 is the wavenumber in vacuum, ε_r is the relative permittivity, σ is the electrical conductivity, ω is the angular frequency, and ε_0 is the permittivity of free space. According to the equation, the complex permittivity $\varepsilon_r - \frac{j\sigma_e}{\omega\varepsilon_0}$ and the relative permeability μ_r serve as intrinsic parameters governing the electromagnetic field distribution. When metal is introduced, its position, shape, orientation, and placement configuration all influence the electromagnetic field distribution.

The interference characteristics of metal on the microwave field can be quantitatively described by the penetration depth, as shown in the following equation[40]:

$$d = \sqrt{\frac{2\rho_e}{\omega\mu_0\mu_{r'}}}, \tag{11}$$

Here, ρ_e denotes the electrical resistivity of the metal, ω represents the microwave frequency, μ_0 is the permeability of free space, and $\mu_{r'}$ is the real part of the complex relative permeability. This equation indicates that microwaves exhibit an extremely shallow penetration depth into metals, with the majority of incident microwave energy reflected at the metal surface. This strong reflectivity renders metals highly effective reflective boundaries within microwave fields. The superposition of incident and reflected waves generates constructive or destructive interference, thereby altering the spatial electromagnetic field distribution. Notably, the ultrasonic probe used in this system measures 50 cm in length, while the wavelength corresponding to a 3 GHz microwave is 10 cm. The comparable electrical dimensions of these two components induce a non-negligible radiation effect, further perturbing the field. In this study, the scanning architecture laterally displaces the metallic probe away from the core irradiation zone of the sample, effectively mitigating both the reflective and radiative effects of the metal. Consequently, the microwave energy distribution within the tissue more closely approximates its intrinsic state, governed solely by the tissue's dielectric properties. Simultaneously, an acousto-optic mirror fabricated from SiO_2 guides the acoustic signal. SiO_2 is a low-loss dielectric material characterized by a low dielectric constant and minimal dielectric loss. It is nearly transparent at microwave frequencies, inducing negligible reflection, scattering, or energy absorption. This design effectively prevents the introduction of extraneous interference within the core irradiation region, preserving the native and consistent distribution of the microwave field in the tissue. This optimization strategy reduces distortion in the electromagnetic energy distribution, thereby providing critical support for rapid and high-fidelity thermoacoustic imaging.

2.4 Field Simulation and Validation

Using CST simulation software, we constructed corresponding electromagnetic models based on the conventional raster scanning approach[11,28] and the mirror-stage hybrid scanning mechanism proposed in this study to evaluate the interference effects of both scanning methods on the microwave field. The simulation model for conventional raster scanning is shown in Fig. 1(a), while the schematic of the mirror-stage hybrid scanning model appears in Fig. 1(c). In both models, red arrows indicate the probe, blue arrows point to the biological tissue, purple arrows denote the dipole antenna, yellow arrows indicate the coupling oil, green arrows mark the mirror, orange arrows indicate the water column, and black arrows point to the copper mesh. The relative permittivity and conductivity values for each component are detailed in Supplementary Table 2 (online). In the conventional raster scanning model, following references [11,28], the biological tissue is positioned 1 mm above the center of the antenna, and the ultrasonic probe is placed 15 mm above the tissue. A water column with a diameter of 12 mm is situated beneath the probe to protect it and facilitate efficient ultrasound transmission. In the mirror-stage hybrid scanning model, the biological tissue is placed directly above the antenna center at a distance of 1 mm, consistent with the actual setup. The scanning module comprises a mirror (21.5 mm × 28.5 mm) and a copper mesh (15 mm in diameter, 28 mm in length), positioned at a 45 ° angle directly above the tissue, with the mirror center located 12.5 mm from the tissue surface. The ultrasonic probe is situated adjacent to the mirror, aligned with the mirror center, and separated from it by a distance of 12.5 mm.

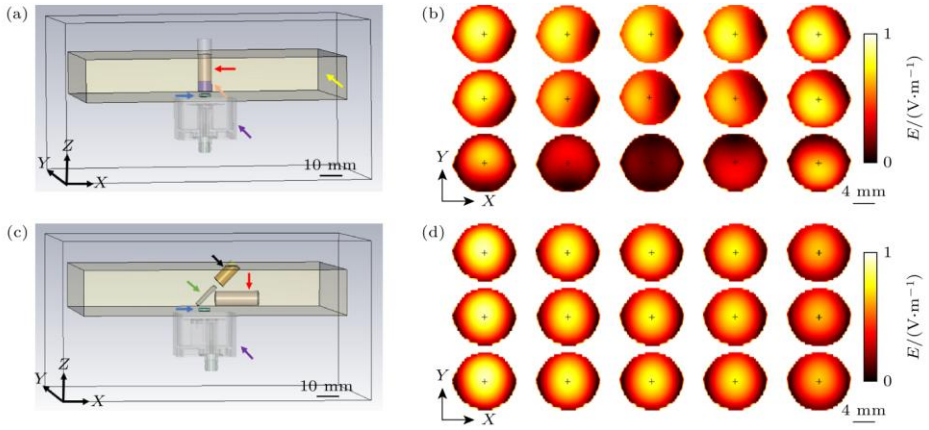

Fig. 1 CST simulation models and electric field (E-field) distribution results: (a) Simulation model under the conventional raster-scanning mechanism; (b) E-field distribution within the tissue corresponding to (a); (c) simulation model under the galvanometer-translational stage hybrid scanning mechanism; (d) E-field distribution within the tissue corresponding to (c)

.

To evaluate the field distribution characteristics within the scanning region, this study established a 5 × 3 asymmetric grid of measurement points over a 14 mm × 14 mm planar area. The coordinates include (7, -7), (3.5, -7), (0, -7), (7, -3.5), (3.5, -3.5), (0, -3.5), (7, 0), (3.5, 0), (0, 0), (7, 3.5), (3.5, 3.5), (0, 3.5), (7, 7), (3.5, 7), and (0, 7) (*Y*, *X*, units: mm). These points were selected to lie unilaterally along the *Y*-axis direction (the galvanometer scanning direction) to avoid potential interpretive bias arising from system symmetry. Figures 1(b) and 1(d) present the electric field distributions at these 15 coordinate points for the conventional raster scanning mechanism and the hybrid galvanometer-translation stage scanning mechanism, respectively. The results show that in Figure 1(b), the electric field distributions differ along both the *X*- and *Y*-axes. In contrast, Figure 1(d) demonstrates superior consistency and higher uniformity along the *Y*-axis, while the electric field intensity along the *X*-axis (translation stage scanning direction) exhibits a slight decreasing trend yet maintains high uniformity. To further quantify these field distribution variations, we computed the structural similarity index measure (SSIM) and mean squared error (MSE) between the electric field distributions at the 14 peripheral points and the central point (0, 0) for both scanning mechanisms. The quantitative results are provided in Supplementary Figure S4 (online). This analysis confirms that the hybrid galvanometer-translation stage scanning mechanism yields more stable and uniform electric field distributions with reduced perturbation to the microwave field.

3 System and Methods

3.1 System Design

The schematic diagram of the proposed rapid microwave-induced thermoacoustic microscopy system is shown in Figure 2. The system employs a 3 GHz microwave source (bandwidth: 50 kHz, peak power: 60 kW, pulse duration: 70 ns, repetition frequency: 100 Hz), which delivers microwaves to the sample via a dipole antenna (dimensions: 6 cm × 6 cm). The resulting average power density on the sample surface is 11.67 mW/cm^2, which remains below the IEEE safety standard (20 mW/cm^2 at 3 GHz). On the detection side, the system adopts an integrated probe design: a custom-molded fixture integrates an ultrasonic transducer (focal length: 25 mm; center frequency: 10 MHz; -6 dB bandwidth: 80%; V311, Olympus) with a scanning galvanometer (custom-built, Scanner Optics Co. Ltd) at a fixed 45 ° angle, ensuring that the transducer's focal plane consistently coincides with the sample surface. The galvanometer provides a mechanical deflection range of ±20 °, corresponding to a minimum scanning span of 14 mm along the *Y*-axis. Coupled with a high-precision translation stage along the *X*-axis (TSA, Zolix), the system achieves

an effective imaging field of view exceeding 14 mm × 14 mm while maintaining constant spatial resolution. The entire integrated module is rigidly mounted on the translation stage. During experiments, both the probe and the sample are fully immersed in transformer oil, which exhibits excellent acoustic and microwave coupling properties. Signals received by the ultrasonic transducer undergo two-stage amplification: first by a low-noise amplifier (CLC-10K0.5G-5510-S, gain: 55 dB, noise figure: 1.0 dB, Suzhou Rebes Electronic Technology Co., Ltd) and then by a pulsed receiver-transmitter with built-in amplification (DPR300, JSR). The amplified signals are subsequently digitized by a data acquisition card (PCI5122, National Instruments) and transferred to a computer for image reconstruction.

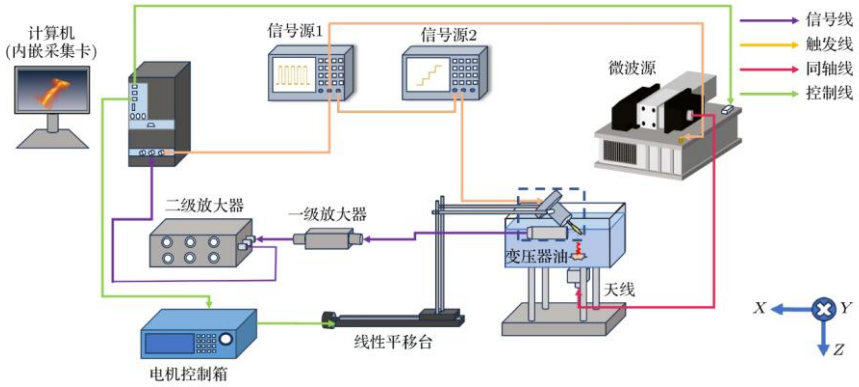

Fig. 2 Schematic of fast microwave-induced thermoacoustic microscopy imaging system.

In microwave-induced thermoacoustic imaging, the signal-to-noise ratio (SNR), penetration depth, contrast, and resolution are all influenced by the characteristics of the microwave pulse. Taking breast cancer as an example (see Supplementary Material Figure S1 (online)), its effective electrical conductivity decreases with decreasing frequency. Consequently, under identical electric field strength, low-frequency excitation yields reduced thermoacoustic signal amplitude and lower SNR. However, low-frequency microwaves experience less attenuation in biological tissues, thereby enhancing imaging depth; conversely, high-frequency microwaves offer higher SNR but limited penetration capability. To balance SNR and penetration depth while ensuring favorable imaging contrast, existing studies predominantly employ microwave excitation within the 1-6 GHz frequency band (see Supplementary Material Table S1 (online)), with frequencies near 3 GHz being most commonly used[41]. This study focuses on accelerating microwave thermoacoustic microscopic imaging to meet the clinical demand for tumor margin detection. Based on the aforementioned considerations, our research team developed a rapid imaging system using a 3 GHz microwave source, enabling efficient image acquisition while maintaining adequate SNR, penetration depth, and contrast. Future work may build upon this foundation by incorporating a multi-frequency fusion strategy to further

enhance lesion detection and identification capabilities.

With the imaging frequency fixed at 3 GHz, system resolution improvement must account for the performance limitations of the microwave source. The microwave source used in this experiment can stably output a minimum pulse width of 70 ns, which excites thermoacoustic signals with a maximum frequency component of approximately 14 MHz, yielding a theoretical axial (*Z*-axis) resolution of about 100 μm. To balance high-frequency resolving capability with low-frequency signal response, this study employs a point-focused ultrasound transducer with a center frequency of 10 MHz and 80% bandwidth. Its frequency response range (6-14 MHz) effectively covers frequencies up to 14 MHz.

Regarding galvanometer selection, high-frequency electromagnetic fields in the microwave environment can interfere with the drive circuitry of MEMS galvanometers (electromagnetically actuated) through spatial radiation, including electromagnetic induction and capacitive coupling, leading to inaccurate control signals. In contrast, laser marking galvanometers-owing to their physically separable structure, higher drive signal strength, superior electromagnetic interference resistance, and inherent electromagnetic shielding provided by their metallic construction-effectively mitigate such interference. Additionally, considering imaging range and cost constraints[31], laser marking galvanometers better suit the requirements of this system. With the ultrasound transducer frequency fixed, a systematic trade-off among focal length, focal spot size, transducer diameter, galvanometer mirror dimensions, and motor specifications is necessary. Conventional galvanometers typically adopt a design featuring large motors paired with small mirrors to achieve high-speed scanning. However, in this system, such a configuration would necessitate an excessively large motor, thereby restricting the usable transducer diameter. Given a fixed transducer focal length and frequency, Equation (9) indicates that the focal spot size would consequently increase, degrading lateral (*X*- and *Y*-axis) resolution. Therefore, this study implements a custom galvanometer design featuring a small motor and a large mirror. In this system, the microwave source operates at a repetition frequency of 100 Hz. Based on a scanning step size of 0.14 mm × 0.2 mm and a field of view of 5 mm × 5 mm, the required maximum scanning rate is calculated as 0.056 Hz. The custom galvanometer system achieves a scanning rate exceeding 1 Hz, fully satisfying practical operational demands. After finalizing the motor and mirror dimensions (motor diameter: 14 mm; mirror size: 28.7 mm × 21.5 mm), the transducer diameter was further determined according to geometric constraints to ensure that, when mounted horizontally, the lower edge of the transducer does not extend beyond the lower boundary of the galvanometer mirror. This prevents an increase in imaging distance due to sample repositioning downward,

which would otherwise degrade resolution. Ultimately, with the focal length fixed, an appropriate transducer diameter (16.5 mm) was selected, resulting in a system focal spot size of 300 μm. Building upon this parameter design, an integrated mold combining the transducer and galvanometer was developed. The galvanometer motor circuitry is housed in an aluminum casing, externally wrapped with copper foil and overlaid with copper mesh (mesh aperture: 74 μm, significantly smaller than the wavelength of the 3 GHz microwaves used in the system, thereby providing substantial attenuation at this frequency). This configuration ensures robust electromagnetic shielding, further guaranteeing stable system operation under microwave interference. Moreover, field distribution control was incorporated into the galvanometer system design from the outset to minimize perturbation of the original microwave field.

3.2 Timing Control

Scanning control and data acquisition timing are jointly implemented by a custom LabVIEW program and a signal generator (DG4062, RIGOL), as illustrated in Figure 3. The system first configures acquisition parameters and initializes the trigger timing of the signal generator via LabVIEW. Subsequently, the signal generator acts as the master clock source, synchronously triggering microwave pulse emission and data acquisition card sampling. The system employs a hybrid acquisition mode combining "point-by-point averaging" with "continuous scanning." Specific parameter settings are as follows: repetition frequency $f_{\text{rep}} = 100\text{Hz}$, scanning step sizes $\delta_Y = 0.14\text{mm}$ and $\delta_X = 0.2\text{mm}$, field of view $5\text{mm} \times 5\text{mm}$ (corresponding to Y-direction point count $N_Y = 5/\delta_Y \approx 36$, X-direction point count $N_X = 5/\delta_X = 25$, and total acquisition points $N_{\text{points}} = N_X \times N_Y = 900$), and number of averages per point $N_{\text{avg}} = 50$.

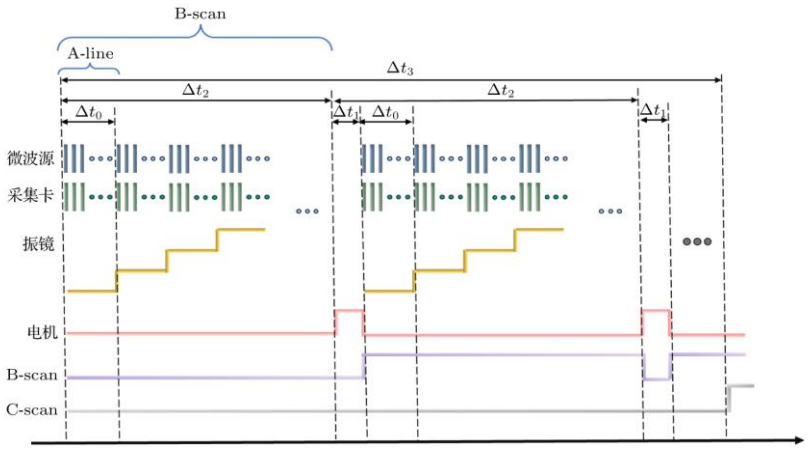

Fig. 3 Timing diagram for fast microwave-induced thermoacoustic microscopy system.

At each scanning position, the signal generator triggers microwave pulses N_{avg} times at a preset repetition frequency, while the data acquisition card synchronously captures the corresponding number of A-line signals. LabVIEW performs real-time signal accumulation and averaging, resulting in a single-point acquisition time of $\Delta t_0 = N_{\text{avg}}/f_{\text{rep}} = 0.5\text{s}$. Upon completing the averaging of the current A-line signal, the galvanometer scanner automatically deflects to the next scanning position to continue data acquisition. This process repeats until $N_Y = 36$ scanning points (i.e., one B-scan frame) are acquired, requiring a total time of $\Delta t_2 = N_{\text{points}} \times \Delta t_0 = 18\text{s}$. The corresponding B-scan acquisition rate is $f_{\text{B-scan}} = 1/\Delta t_2 = 0.056\text{Hz}$. After B-scan acquisition, LabVIEW drives the translation stage via a motor controller to perform a stepping motion, which takes $\Delta t_1 = 0.2\text{s}$. The system iteratively executes this workflow to progressively construct a three-dimensional dataset, with a total system runtime of $\Delta t_3 = N_X \times (\Delta t_2 + \Delta t_1) = 455\text{s}$. Finally, the system invokes a LabVIEW-MATLAB co-interface to generate three-dimensional microwave-induced thermoacoustic microscopic images using a dedicated reconstruction algorithm.

Regarding timing precision, system performance is primarily influenced by three critical factors: galvanometer response time jitter, trigger delay, and timing errors. Concerning galvanometer response, the high-precision laser marking galvanometer employed in the system exhibits an ideal step response time of 100 μs, with actual response time jitter below 5 μs. Given the system's microwave repetition frequency of 100 Hz (pulse interval of 10 ms), both the galvanometer's response time and its jitter are significantly shorter than the acquisition interval; thus, their impact on system timing precision is negligible. In terms of trigger synchronization, the microwave source and data acquisition card are connected via identical BNC cables of equal length to a common trigger source through a T-connector, achieving hardware-level synchronous triggering. This configuration ensures that the microwave trigger signal and the acquisition trigger signal are effectively generated simultaneously, attaining microsecond-level synchronization accuracy. Although thermoacoustic signals require finite time to propagate to the acquisition card-causing the actual signal capture to lag behind the trigger instant-the acquisition card enters a blocking state upon triggering (with a blocking duration exceeding 10 ms), during which it reliably captures the signal. Given the mature manufacturing process of BNC transmission cables, their propagation delay is less than 10 ns/m; with 2 m cables used in the system, the total transmission delay remains below 20 ns, which is far shorter than the acquisition card's blocking time. Consequently, this delay exerts a negligible effect on system timing precision. Regarding timing errors, the system's timing accuracy primarily depends on the timebase precision of the signal generator (typical value: 2 ppm,

where 1 ppm = 10^{-6}). Under a 100 Hz repetition frequency, the cumulative timing error for acquiring a single A-line is approximately 1 ns, and the cumulative error over an entire B-scan acquisition is about 100 ns. Additionally, the cumulative period error for the galvanometer to complete one B-scan (with a period of approximately 50 s) is roughly 100 μs. Combining trigger signal errors and galvanometer motion errors, the total B-scan timing error amounts to approximately 100.1 μs, which is substantially smaller than the pulse trigger interval (10 ms). Therefore, within a single B-scan acquisition cycle, this timing error has a negligible impact on system performance. Moreover, the system re-synchronizes its timing after each B-scan acquisition, preventing error accumulation across multiple B-scans and thereby ensuring long-term timing stability.

3.3 Image Reconstruction

Conventional microwave-induced thermoacoustic microscopic imaging typically employs point-by-point linear scanning with an ultrasonic transducer for signal acquisition, as illustrated in Supplementary Material Figure S4(a) (online). In this model, the acquired data matrix directly corresponds to a Cartesian coordinate system; that is, the data storage model aligns with the data acquisition model, enabling direct processing of the data matrix to reconstruct three-dimensional images and generate maximum intensity projection images. However, this study adopts a galvanometer-based fan-shaped scanning mechanism, as depicted in Supplementary Material Figure S4(b) (online). Under this mechanism, the actual acquired data exhibit a wedge-shaped distribution. If the rectangular storage model were directly applied for image reconstruction, the actual fan-shaped data would be erroneously compressed into a rectangular volume referenced to the smallest upper surface, resulting in geometric distortion inconsistent with the true data. Therefore, during image reconstruction, the data storage model-initially corresponding to the rectangular model shown in Supplementary Material Figure S4(a) (online)-must be transformed into the frustum model illustrated in Supplementary Material Figure S4(b) (online). This alignment between the data storage model and the data acquisition model enables effective distortion correction.

Let the original data storage matrix be denoted as $D \in \mathbb{R}^{N_X \times N_Y \times N_Z}$, where N_X represents the number of acquisition points along the X-axis, N_Y denotes the number of acquisition points along the Y-axis, and N_Z indicates the number of sampling points along the acoustic propagation direction. For each element $D_{k,i,j}$ in the matrix, its three-dimensional spatial coordinates $(X_k, Y_{i\ \ j}, Z_{ij})$ can be determined by the following equation:

$$\begin{matrix} X_k = (k-1)\cdot\delta_X, & k \in \{1,2,\cdots,N_Y\}, \\ \{Y_{i,j} = \rho_{i,j}\cdot\sin\vartheta_i - d_{\text{offset}}, & i \in \{1,2,\cdots,N_Y\}, \\ Z_{i,j} = \rho_{i,j}\cdot\cos\vartheta_i - d_{\text{offset}}, & j \in \{1,2,\cdots,N_Z\}, \end{matrix} \quad (12)$$

Here, δ_X denotes the sampling interval along the X-axis (unit: mm), d_{offset} represents the linear distance between the galvanometer and the probe (unit: mm), $\rho_{i,j}$ indicates the effective propagation distance of the thermoacoustic signal at the jth sampling point, which can be described by Equation (13), and ϑ_i denotes the current scanning angle, as expressed in Equation (14):

$$\rho_{i,j} = j\cdot\delta_{\text{p}} + s_{\text{start}}\cdot\delta_{\text{p}}, \quad (13)$$

$$\vartheta_i = -\frac{\Phi}{2} + (i-1)\cdot\frac{\Phi}{N_Y-1}, \quad (14)$$

Here, s_{start} denotes the starting sampling point of the acoustic axis, Φ represents the maximum deflection angle of the galvanometer mirror (in degrees (°)), and δ_{p} indicates the sampling interval along the acoustic axis, which can be expressed by Equation (15):

$$\delta_{\text{p}} = c\times 1000/f_{\text{s}}, \quad (15)$$

Here, c denotes the speed of sound (unit: m/s), and f_{s} denotes the sampling rate of the data acquisition card (unit: Hz).

Mapping the maximum value directly based on actual coordinates compromises both spatial and temporal efficiency of the algorithm. Therefore, the maximum value within a defined neighborhood around the exact sampling point can serve as the representative value for the current region. The value at $(X_k, Y_{i\ ,j}, Z_{i,\ j})$ can then be expressed by Equation (16):

$$\begin{matrix} M(X_k, Y_{i,j}, Z_{i,j}) \\ = \quad max\{D_{k,i,j} | i \in \lfloor\frac{\vartheta}{\Delta\vartheta}\rfloor + \{0,1\},\} \\ j \in \lfloor\frac{Z}{\delta_p}\rfloor + \{0,1\}, \end{matrix} \quad (16)$$

Here, $\Delta\theta$ denotes the angular spacing, which can be expressed by Equation (17):

$$\Delta\vartheta = \Phi/(N_Y - 1). \quad (17)$$

Following data reconstruction, a three-dimensional feature matrix is obtained. By extracting the maximum value from each A-line signal and projecting it onto the XY

plane, a two-dimensional maximum intensity projection matrix is generated.

The image reconstruction algorithm optimized according to the above equations for the galvanometer-based sector scanning mode employs an efficient approximation strategy. While this approach enhances computational speed, it also introduces certain image artifacts. These artifacts arise from error coupling between two sequential processing stages. The front-end coordinate mapping process (Equations (12)-(15)) involves floating-point trigonometric calculations, which introduce non-uniform positional mapping errors. Consequently, signal values are assigned to grid points that deviate from their true physical locations. The back-end maximum intensity projection strategy (Equation (16)) further amplifies this error. This strategy essentially forgoes searching for the theoretically exact position and instead selects the strongest signal response within a fixed neighborhood. Therefore, any strong reflective signal displaced into the vicinity of a grid point due to front-end mapping inaccuracies is captured by the algorithm and erroneously aggregated to the same projection location. This ultimately manifests in the image as ghosting or trailing artifacts. In this study, major system distortions were uniformly corrected through a data-driven model. The subtle artifacts resulting from the trade-off between numerical precision and computational efficiency can be suppressed through standard image processing procedures (see Supplementary Material Figure S2(e) (online) for the relevant processing pipeline; for comparisons of data before and after processing, refer to Supplementary Material Figure S2 (online) and Figure 4 in the main text, respectively).

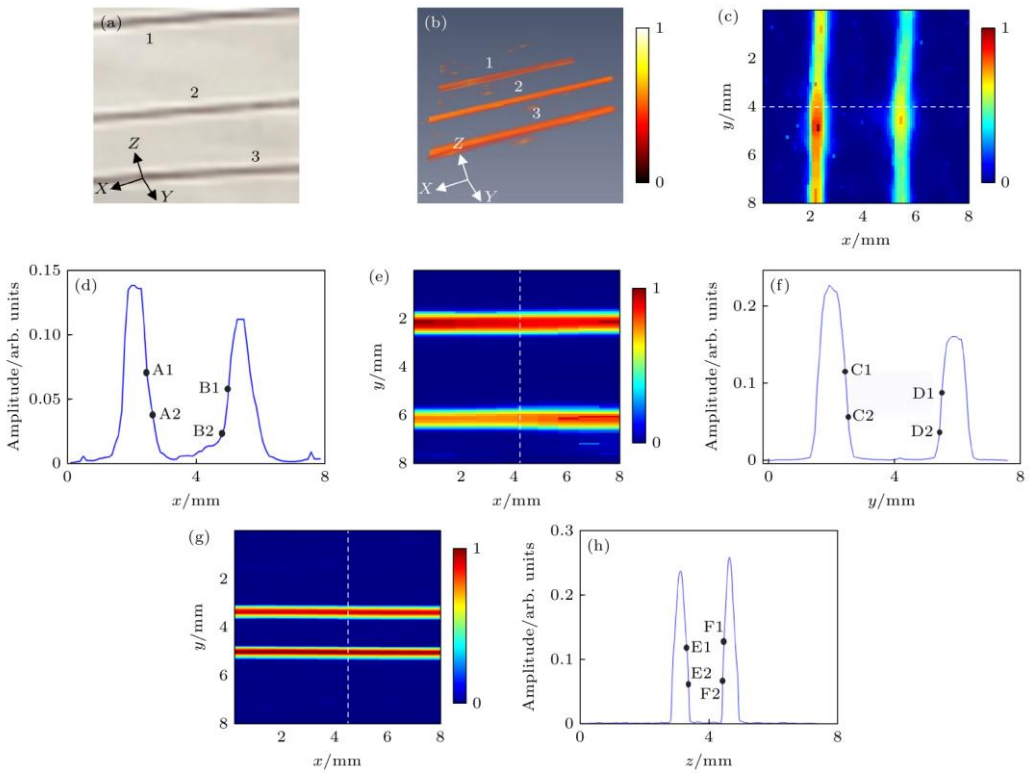

Fig. 4 Copper wire experiment: (a) Photograph of 90 μm-diameter copper wires; (b) 3D FTAM image; (c) 2D FTAM images of copper wires 1 and 2 along the z-axis for *X*-axis resolution testing; (d) thermoacoustic signal profile along the white dashed line in (c); (e) 2D FTAM images of copper wires 1 and 2 along the *Z*-axis for *Y*-axis resolution testing; (f) thermoacoustic signal profile along the white dashed line in (e); (g) 2D FTAM images of copper wires 2 and 3 along the *Y*-axis for *Z*-axis resolution testing; (h) thermoacoustic signal profile along the white dashed line in (g).

4 Experimental Results and Discussion

4.1 Copper Wire Experiment

To evaluate the three-dimensional resolution characteristics of the system, three copper wires, each with a diameter of 90 μm, were arranged in parallel as illustrated in Fig. 4(a). The specific configuration is as follows: Wires 1 and 2 were positioned horizontally and coplanar, with a center-to-center spacing of 3 mm; wires 2 and 3 were arranged vertically and coplanar, with a spacing of 2 mm. The planes containing these two wire pairs are mutually orthogonal. Figure 4(b) presents the corresponding three-dimensional MITAM image (the unfiltered raw image is provided in Fig. S2 of the online supplementary material). For *X*-axis resolution testing, the copper wires were oriented perpendicular to the *X*-axis (i.e., parallel to the *YZ* plane). Figure 4(c) shows the two-dimensional MITAM projection image of wires 1 and 2 along the *Z*-axis, and Fig. 4(d) displays the thermoacoustic signal profile along the white dashed

line. Following the standard resolution calculation method described in Ref. [42], we first identified the points at half-maximum amplitude (points A_1 and B_1) and quarter-maximum amplitude (points A_2 and B_2) on the profile curve. The distances between A_1 and A_2, and between B_1 and B_2, were measured separately. Summing these two distances yielded an X-axis resolution of 332 μm.

Similarly, for *Y*-axis resolution testing, the copper wires were aligned perpendicular to the *Y*-axis (i.e., parallel to the *XZ* plane). Figure 4(e) shows the two-dimensional MITAM projection image of wires 1 and 2 along the *Z*-axis, and Fig. 4(f) presents the corresponding signal profile. Applying the same resolution calculation method used for the *X*-axis, the *Y*-axis resolution was determined to be 324 μm. For *Z*-axis resolution testing, the wires were oriented perpendicular to the *Z*-axis (i.e., parallel to the *XY* plane). Figure 4(g) displays the two-dimensional MITAM projection image of wires 2 and 3 along the *Y*-axis, and Fig. 4(h) shows the corresponding signal profile. Using the identical calculation approach, the *Z*-axis resolution was found to be 79 μm.

The experimental results indicate that the measured resolutions of 332 μm along the *X*-axis and 324 μm along the *Y*-axis align well with the theoretical focal spot diameter of 300 μm, with deviations falling within the expected range. During the experiment, when the transducer was moved within the focal length range, ultrasonic attenuation and the fact that the actual acoustic focal spot size at the sample plane typically exceeds the theoretical value led to a slight degradation in measured resolution. Along the *Z*-axis, the theoretical resolution calculated from the 70 ns pulse width is approximately 100 μm, whereas the experimentally measured value is about 79 μm. This discrepancy primarily arises because the actual output pulse width is slightly shorter than the set value, causing the theoretically calculated resolution based on pulse width to be overestimated. Moreover, considering that the half-wavelength of the ultrasound transducer sets a fundamental resolution limit of approximately 55 μm, the experimentally obtained *Z*-axis resolution demonstrates good agreement with theoretical expectations, confirming the consistency between the theoretical model and actual imaging performance.

Additionally, spatial non-uniformity is observed in the copper wire signals in Fig. 4(c), and differences exist between the signals in Figs. 4(c) and 4(e). These phenomena stem from the physical mechanisms of microwave-metal interaction and variations in the imaging environment. Specifically, during microwave-induced thermoacoustic imaging, the electromagnetic response of the copper wire resembles that of an antenna[43,44]: the microwave field drives surface charges on the copper wire to generate induced currents. Consequently, the metal wire absorbs electric field energy and undergoes localized heating. Although the thermal expansion of the copper wire

itself is negligible, it periodically heats the surrounding medium, inducing periodic pressure variations that generate spherical acoustic waves. The non-uniform image distribution in Fig. 4(c) can be explained from two perspectives: first, the electromagnetic effect produced by microwaves acting on the copper wire depends on the wire's position within the dipole antenna's radiation field; second, the secondary electromagnetic fields generated by any two wires as secondary radiators superimpose with the original microwave field at the location of the third wire, potentially enhancing or attenuating the local field strength. The differences between the two images primarily result from environmental changes during sample acquisition. Figure 4(c) shows the imaging result obtained as the copper wire sample was translated along the stage motion direction (i.e., perpendicular to the galvanometer rotation axis) for *X*-axis resolution calculation, whereas Fig. 4(e) displays the image acquired from the same sample rotated along the galvanometer rotation direction (i.e., perpendicular to the stage motion direction) for *Y*-axis resolution calculation. Although both images originate from the same copper wire sample, the sample must be rotated by 90 °after acquiring Fig. 4(c) to obtain Fig. 4(e). During this rotation, it is difficult to maintain the exact relative position between the copper wires and the antenna, resulting in differences in the microwave field distribution experienced by the sample during the two imaging sessions and thus causing the observed discrepancies between Figs. 4(c) and 4(e).

4.2 Saline Tube Imaging

To validate the system's contrast performance, capillary tubes with an inner diameter of 0.2 mm were used to prepare saline samples at concentrations of 2% and 3%. As shown in Fig. 5(a), sample 1 corresponds to the 2% concentration, and sample 2 to the 3% concentration. The two-dimensional MITAM image acquired by the system is presented in Fig. 5(b), clearly revealing the morphological features of both saline tubes. Figure 5(c) plots the pixel values from selected regions of the two saline tubes in Fig. 5(b) alongside their theoretical equivalent electrical conductivities[45,46]. The experimental results demonstrate that the thermoacoustic signal amplitudes of the 2% and 3% saline solutions increase with higher equivalent electrical conductivity, following a similar trend. However, the actual ratio of their signal amplitudes deviates from the theoretical ratio. This discrepancy is primarily attributed to the spatial non-uniformity of the microwave field within the imaging region. As indicated by Eqs. (1) and (2), the thermoacoustic signal intensity is governed by the local heating function, which is directly influenced by the spatial distribution of microwave energy, causing samples at different spatial locations to absorb varying amounts of microwave energy. Furthermore, inevitable fluctuations in saline concentration during manual

preparation of the tubes introduce additional inter-sample variability.

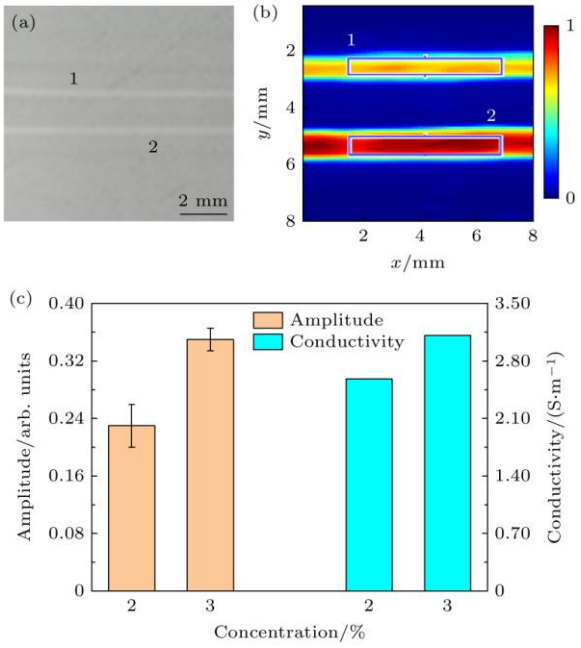

Fig. 5 Saline tube experiment: (a) Photograph of saline tubes with 0.2 mm inner diameter; (b) 2D FTAM image; (c) statistical results of pixel values in the selected region from (b), with theoretical electrical conductivity values for tubes containing 2% and 3% saline concentrations.

Overall, the system qualitatively reflects the differences in equivalent conductivity among saline tubes of varying concentrations, confirming its strong contrast imaging capability.

4.3 Depth Imaging

To evaluate the system's imaging performance along the depth dimension, the experiment employed three saline tubes, each with a concentration of 10%, positioned at different depths, and prepared two sample groups. The first sample group is shown in Figure 6(a), where the depth intervals between tubes 1 and 2 and between tubes 2 and 3 are each approximately 5 mm. All saline tubes were fabricated in air. During actual imaging, the entire sample was immersed in transformer-coupled oil for measurement. As shown in the three-dimensional and two-dimensional microwave-induced thermoacoustic images in Figure 6(b), signals from all three saline tubes are clearly identifiable. The second sample group is illustrated in Figure 6(c), where the depth intervals between tubes 4 and 5 and between tubes 5 and 6 are also approximately 5 mm, and all saline tubes are embedded within adipose tissue approximately 13 mm thick. During imaging, this sample was likewise fully immersed in transformer oil. The three-dimensional and two-dimensional microwave-induced thermoacoustic images in Figure 6(d) reveal signals from all three

saline tubes, although the signal from the third tube (tube 6) exhibits some attenuation.

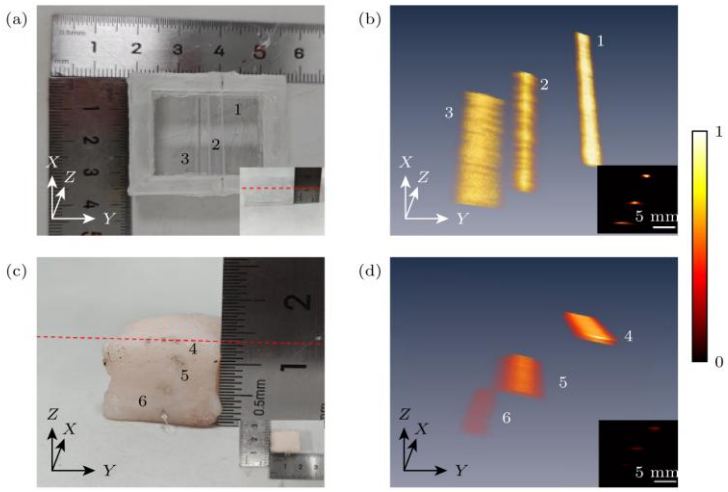

Fig. 6 Depth imaging: (a) Photograph of the sample placed in air; (b) corresponding 3D and 2D microwave-induced thermoacoustic images of the sample in (a); (c) photograph of the sample embedded in fat; (d) corresponding 3D and 2D microwave-induced thermoacoustic images of the sample in (c).

Experimental results from both groups indicate that the effective detection depth of microwave-induced thermoacoustic imaging in biological tissues is reduced compared to that in air, yet remains no less than 10 mm. Furthermore, as shown in Fig. 6(b), signals from deeper saline tubes exhibit broadening. This phenomenon primarily stems from the acoustic characteristics of the point-focused ultrasound transducer employed: away from the focal plane, the focal spot size gradually increases, leading to a reduction in lateral resolution with increasing depth. This effect could be mitigated through the subsequent development of specialized algorithms. In Fig. 6(d), certain signals display further broadening compared to those in Fig. 6(b), likely due to deformation of the saline tubes caused by compression during embedding in fat tissue. The absence of noticeable broadening in the signal from saline tube No. 6 may be attributed to its greater burial depth, which prevents weaker surrounding thermoacoustic signals from penetrating the tissue and reaching the transducer.

It should be emphasized that imaging depth is not directly correlated with imaging speed. The system's imaging depth primarily depends on microwave energy characteristics, ultrasound propagation properties, and transducer performance parameters. The ultrasound transducer used in this system has a depth of field of 4 mm within the -6 dB range. At a depth of 10 mm-beyond the optimal depth-of-field range-the system still maintains a favorable signal-to-noise ratio, enabling effective imaging despite a reasonable decline in spatial resolution. Consequently, the phantom experiments in this study were confined to depths around 10 mm, and deeper

measurements were not performed. To further enhance imaging depth, one could consider employing an ultrasound transducer with a larger depth of field and, if necessary, pairing it with a microwave source delivering higher pulse power. However, such improvements would require more extensive design and optimization based on the current system.

4.4 Early-Stage Tumor Simulated Imaging

To validate the system's imaging potential in biological tissues, simulated early-stage tumor imaging experiments were conducted. Taking breast cancer as an example, tumor tissue typically exhibits higher electrical conductivity than surrounding adipose tissue. In theory, microwave-induced thermoacoustic imaging can therefore generate high-contrast images for effective lesion detection. Following references [47,48], fresh pork belly was used as a phantom sample. A thin muscle layer together with its surrounding fat tissue was excised to mimic a breast tumor and adjacent normal tissue. The muscle tissue measured 3 mm in width and exhibited an elongated structure, as illustrated in Fig. 7(a). Comparative experiments were performed on the sample using both ultrasound microscopy and rapid thermoacoustic microscopy.

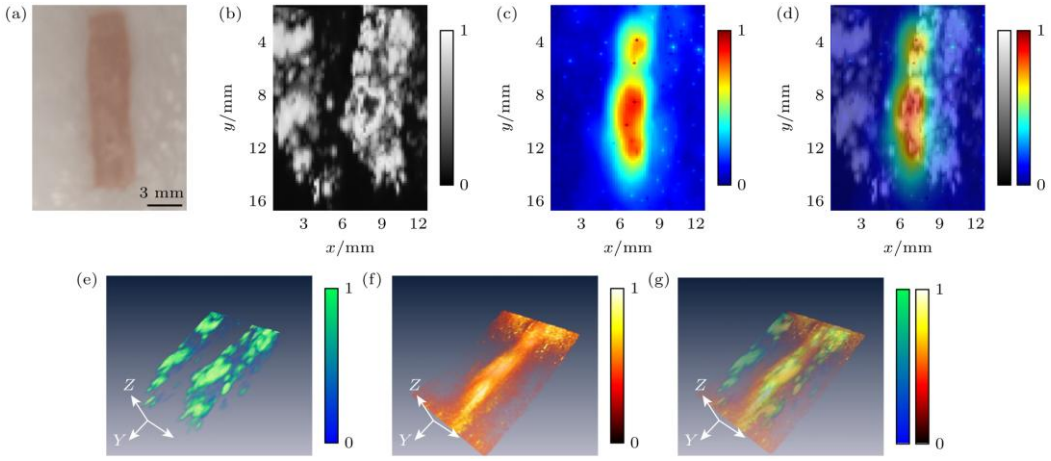

Fig. 7 Early-stage tumor simulation imaging: (a) Photograph of the phantom; (b) 2D ultrasound image; (c) 2D thermoacoustic microscopy (TAM) image; (d) 2D thermoacoustic-ultrasound image; (e) 3D ultrasound image; (f) 3D TAM image; (g) 3D thermoacoustic-ultrasound image.

In the ultrasound imaging results, Figures 7(b) and (e) display the two-dimensional (2D) and three-dimensional (3D) images, respectively. Combined structural analysis of the physical specimen reveals that the ultrasound signal exhibits strong responses in certain lesion regions, yet appears weaker than in non-lesion regions in other areas. Signal interference from adipose tissue compromises accurate lesion localization. Moreover, ultrasound signals are predominantly confined to the surface region of the sample, demonstrating limited capability for capturing internal signals. In contrast,

thermoacoustic microscopic imaging results, shown in Figures 7(c) and (f), clearly delineate both lesions and their boundary features in 2D and 3D representations. Adipose tissue exerts minimal interference on thermoacoustic imaging, and the system provides richer depth information. Figures 7(d) and (g) further illustrate the fused 2D and 3D images combining ultrasound and thermoacoustic modalities. Experimental results indicate that although ultrasound imaging possesses certain tumor detection capability, it suffers significant interference from adipose tissue and struggles to accurately define tumor margins. Thermoacoustic imaging demonstrates superior performance in tumor detection, exhibiting minimal susceptibility to adipose interference and clearly resolving boundary regions, thereby validating the potential of this microwave-induced thermoacoustic microscopy (MITAM) technique for rapid assessment of early tumor margins.

5 Conclusion

This study proposes and implements a microwave-induced thermoacoustic microscopic imaging system based on one-dimensional galvanometer scanning. A cooperative scanning strategy combining a galvanometer mirror and a translation stage enables 3D imaging. Classic resolution and contrast validation experiments from the microwave-induced thermoacoustic imaging field-specifically, copper wire resolution tests and saline tube contrast assessments[4,49,50]-demonstrate that the system achieves a B-scan imaging speed of 18 s per frame (with a 100 Hz pulse repetition frequency, step sizes of 0.14 mm × 0.2 mm, and a 5 mm × 5 mm field of view, equivalent to a frame rate of 0.056 Hz) while maintaining robust imaging performance. The copper wire experiment yields a system resolution of 332 μm × 324 μm × 79 μm. Contrast experiments using saline tubes at different concentrations (2% and 3%) confirm the system's strong contrast resolution capability. Simulated tumor experiments further validate the system's imaging efficacy in biological tissues, preliminarily demonstrating its potential for rapid tumor margin detection. Performance validation based on phantom and ex vivo tissue experiments establishes essential benchmarks and experimental foundations for future development of a two-dimensional galvanometer scanning architecture integrated with a reflection-mode thermoacoustic microscopic imaging scheme to enable in vivo studies.

Regarding imaging performance, both imaging depth and signal-to-noise ratio (SNR) hold potential for further improvement. Specifically, introducing a metallic reflector structure during microwave excitation[47] can optimize electromagnetic field distribution, thereby effectively enhancing imaging depth and signal strength without

compromising other system performance metrics. Additionally, integrating classical algorithms or developing novel image reconstruction methods could further improve image SNR and structural integrity, collectively optimizing overall system performance. Moreover, photoacoustic imaging (PAI), a widely studied technique, typically offers higher spatial resolution and SNR[51-53]. Its tomographic mode achieves centimeter-scale imaging depth[51], whereas its microscopic mode is generally limited to millimeter-scale penetration[51,53-55]. In contrast, microwave-induced thermoacoustic imaging (MITAI), which uses microwaves as the excitation source, overcomes the optical penetration depth limitation. Its tomographic mode enables deep-tissue imaging at depths of tens of centimeters[52]. As shown in the depth imaging experiment in Figure 6 of this study, the microscopic mode achieves a penetration depth of at least 10 mm. Since both MITAI and PAI fundamentally generate ultrasound waves and rely on ultrasound detection for image formation, they can share a common data acquisition and processing module. This compatibility reduces image registration complexity and integration costs, offering inherent advantages for multimodal fusion. Leveraging these characteristics, future work may develop a dual-modality imaging system that combines the high resolution of photoacoustic microscopy with the deep penetration capability of microwave-induced thermoacoustic microscopy, integrating both optical absorption and microwave dielectric absorption properties of biological tissues to enable functional observation of microscopic structures in deep tissues.

In terms of imaging speed, the system's scanning efficiency is primarily constrained by the microwave source's pulse repetition frequency and the number of signal averages required per A-line, i.e., maximum scanning rate = repetition frequency / number of averages. The number of averages is mainly determined by SNR, which in turn depends on microwave field stability and field strength. As shown in the simulation results in Figure 1, the proposed hybrid galvanometer-translation stage scanning mechanism effectively reduces interference with the microwave field. This reduction in interference during scanning concurrently mitigates the adverse feedback effect of microwave field instability on the system, thereby decreasing the required number of signal averages and improving imaging efficiency. Given the current system's noise level, 40-50 signal averages per A-line remain necessary to ensure image quality. As illustrated in Supplementary Material Figure S5 (online), the SNR of raw copper wire signals under conventional raster scanning with 500 averages is 15.59 dB, whereas the proposed system achieves an SNR of 13.77 dB with only 50 averages. This suggests that the SNR per single excitation in the latter is at least comparable to that of the former. This level of averaging ensures sufficient image quality to clearly distinguish samples with conductivities of 2.58 S/m (2%

concentration) and 3.11 S/m (3% concentration), as shown in Figure 5. The absolute difference is 0.53 S/m, with a relative ratio of 1:1.21. Based on this result, the preliminary imaging system can sensitively resolve conductivity differences of at least 0.53 S/m, indicating a conductivity resolution of no less than 0.53 S/m. Currently, further improvements in scanning speed remain fundamentally limited by the microwave pulse repetition frequency, which directly determines the maximum number of excitations per unit time and thus strictly constrains the galvanometer's maximum scanning rate. Employing a microwave source with a higher repetition frequency would further enhance imaging speed.

Furthermore, although the introduction of galvanometer scanning effectively reduces interference with the microwave field during scanning and improves imaging speed, the retained one-dimensional translation stage still induces localized microwave field disturbances. To further increase speed, future research could explore alternative architectures such as two-dimensional galvanometer systems or polygonal mirror scanning mechanisms[56,57] to replace the current hybrid approach. However, such solutions require in-depth investigation of their interaction mechanisms with the microwave field, along with the development of corresponding control timing protocols and image reconstruction algorithms. These approaches would also introduce new challenges regarding system complexity, electromagnetic compatibility, and cost. This study provides a feasibility foundation for subsequent iterations of scanning technology, and future work will focus on exploring more efficient and practical scanning strategies based on the current framework.

References

[1] Bell A G 1880 *Am. J. Sci*. **s3-20** 305

[2] Olsen R G, Lin J C 1983 *Bioelectromagnetics* **4** 397

[3] Kruger R A, Kopecky K K, Aisen A M, Reinecke D R, Kruger G A, Kiser W L 1999 *Radiology* **211** 275

[4] Ku G, Wang L V 2000 *Med. Phys.* **27** 1195

[5] Kruger R A, Miller K D, Reynolds H E, Kiser W L, Reinecke D R, Kruger G A 2000 *Radiology* **216** 279

[6] Singhvi A, Boyle K C, Fallahpour M, Khuri-Yakub B T, Arbabian A 2019 *IEEE Trans. Ultrason. Ferroelectr. Freq. Control* **66** 1587

[7] Ren M Y, Cheng Z W, Wu L H, Zhang H M, Zhang S X, Chen X Y 2022 *IEEE Trans. Biomed. Eng.* **70** 175

[8] Wu L H, Cheng Z W, Ma Y Z, Li Y J, Ren M Y, Xing D, Qin H 2021 *IEEE Trans.*

Med. Imaging **41** 1080

[9] Zhao S X, Wang H H, Li Y J, Nie L M, Zhang S X, Xing D, Qin H 2021 *IEEE Trans. Biomed. Eng.* **69** 725

[10] Liang X, Guo H, Liu Q, Wu C F, Gong Y B, Xi L 2020 *Appl. Phys. Lett.* **116** 013701

[11] Chen Y, Chi Z H, Du S, Fang Q C, Jiang H B 2024 *Appl. Phys. Lett.* **124** 163702

[12] Xu M H, Xu Y, Wang L H V 2003 *IEEE Trans. Biomed. Eng.* **50** 1086

[13] Wan P C, Liu S L, Tian R P, Shang X, Peng W T 2023 *J. Appl. Phys.* **133** 103101

[14] Liu S L, Zheng Z, Sun X X, Zhao Z Q, Zheng Y J, Jiang H B 2019 *IEEE Trans. Biomed. Eng.* **67** 2206

[15] Luo Z X, Li C Z, Liu D T, Wang B S, Zhang L J, Ma Y X 2023 *IEEE Trans. Microw. Theory Tech.* **71** 2652

[16] Evans A L, Ma C, Hagness S C 2022 *Biomed. Phys. Eng. Express* **8** 035020

[17] Mast T D, Johnstone D A, Dumoulin C L, Lamba M A, Patch S K 2023 *Phys. Med. Biol.* **68** 025003

[18] Kruger R A, Kiser W L, Reinecke D R, Kruger G A, Miller K D 2003 *Mol. Imaging* **2** 113

[19] Chi Z H, Huang L, Wu D, Long X J, Xu X L, Jiang H B 2022 *Med. Phys.* **49** 84

[20] Huang L, Zheng Z, Chi Z H, Jiang H B 2021 *Med. Phys.* **48** 4242

[21] Xiang H J, Zheng Z, Huang L, Qiu T T, Luo Y, Jiang H B 2021 *Med. Phys.* **48** 1608

[22] Kellnberger S, Hajiaboli A, Razansky D, Ntziachristos V 2011 *Phys. Med. Biol.* **56** 3433

[23] Tamimi E A, Xin H, Witte R S 2020 *Appl. Opt.* **59** G255

[24] Liu S L, Shang X, Lu Y X, Huang L 2022 *Appl. Phys. Lett.* **121** 243701

[25] Xi Z J, Wang X Y, Ye K, Wang X 2023 *IEEE J. Electromagn. RF Microw. Med. Biol.* **7** 383

[26] Wang X Y, Xi Z J, Ye K, Gong Z, Chen Y F, Wang X 2024 *Sensors* **24** 2682

[27] Lou C G, Yang S H, Ji Z, Chen Q, Xing D 2012 *Phys. Rev. Lett.* **109** 218101

[28] Fang Q C, Chi Z H, Liu Y, Wang Y, Du S, Wu D, Jiang H B 2023 *Med. Phys.* **50** 6036

[29] Chen S L, Xie Z X, Ling T, Guo L J, Wei X B, Wang X D 2012 *Opt. Lett.* **37** 4263

[30] Yao J J, Huang C H, Wang L D, Yang J M, Gao L, Maslov K I, Zou J, Wang L H V 2012 *J. Biomed. Opt.* **17** 080505.

[31] Xu S Z, Xie S M, Wu D, Chi Z H, Huang L 2022 Acta Phys. Sin. 71 050701

[32] Zhu K G, Popovic M 2009 *IEEE Antennas Wirel. Propag. Lett.* **8** 1259
[33] Wang Y, Zhang H M, Qin H 2023 *Acta Phys. Sin.* **72** 204301
[34] Wang L H V, Zhao X M, Sun H T, Ku G 1999 *Rev. Sci. Instrum.* **70** 3744
[35] Zhu G K, Popovic M 2011 *Prog. Electromagn. Res. B* **35** 1
[36] Calasso I G, Craig W, Diebold G J 2001 *Phys. Rev. Lett.* **86** 3550
[37] Gusev V E, Karabutov A A 1993 *Laser Optoacoustics* （New York: AIP Press） pp1–12
[38] Imasonic https://www.imasonic-ndt.com/online-design/ [2025-07-20].
[39] Sonic Concepts https://www.sonicconcepts.com/transducer-selection-guide-single-element/ [2025-07-25].
[40] Sun J, Wang W L, Yue Q Y 2016 *Materials* **9** 231
[41] Benny R, Anjit T A, Mythili P 2020 *Prog. Electromagn. Res. B* **87** 61
[42] Xu M, Xu Y, Wang L V 2003 IEEE Transactions on Biomedical Engineering 50 1086-1099
[43] Liang Z, Wang W P, Qiao S Q, Huang L 2022 *J. Innov. Opt. Health Sci.* **15** 2250015
[44] Niskanen A O, Hassel J, Tikander M, Maijala P, Grönberg L, Helistö P 2009 *Appl. Phys. Lett.* **95** 163701
[45] Yang X Q, Huang K M 2006 *Acta Electron. Sin.* **34** 356
[46] Zhang W T, Chen X, Wang Y, Wu L Y, Hu Y D 2010 *Res. Explor. Lab.* **29** 159
[47] Du S, Qiang T, Chi Z H, Jiang H B 2024 *J. Innov. Opt. Health Sci.* **17** 2450014
[48] Du J S, Gao Y, Bi X, Qi W Z, Huang L, Rong J 2015 *Acta Phys. Sin.* **64** 034301
[49] Xie S M, Huang L, Wang X, Chi Z H, Tang Y H, Zheng Z, Jiang H B 2021 *J. Mech. Eng.* **70** 100701
[50] Cheng Z W, Wu L H, Qiu T S, Duan Y H, Qin H, Hu J 2021 *IEEE Trans. Med. Imaging* **40** 3498
[51] Zhang Y M, Wang F, Lin L, Ye J 2024 *J. Instrum. Anal.* **43** 19
[52] Tang X Y, Fu J, Qin H 2023 *J. Innov. Opt. Health Sci.* **16** 2230014
[53] Sun M L, Li C Y, Chen R M, Shi J H 2024 *Laser Optoelectron. Prog.* **61** 0618017
[54] Jeon S, Kim J, Lee D, Baik J W, Kim C 2019 *Photoacoustics* **15** 100141
[55] Chen Z J, Yang S H, Xing D 2018 *Chin. J. Lasers* **45** 0307008
[56] Kim J Y, Lee C, Park K, Lim G, Kim C 2015 *Sci. Rep.* **5** 7932
[57] Qi W Z, Jin T, Rong J, Jiang H B, Xi L 2017 *J. Biophotonics* **10** 1580